ACS APPLIED MATERIALS & INTERFACES

www.acsami.org

Research Article

Nanoscaled $LiMn_2O_4$ for Extended Cycling Stability in the 3 V Plateau

Valerie Siller, Juan Carlos Gonzalez-Rosillo, Marc Nuñez Eroles, Federico Baiutti, Maciej Oskar Liedke, Maik Butterling, Ahmed G. Attallah, Eric Hirschmann, Andreas Wagner, Alex Morata,* and Albert Tarancón*

Cite This: *ACS Appl. Mater. Interfaces* 2022, 14, 33438−33446

Read Online

ACCESS | Metrics & More | Article Recommendations | Supporting Information

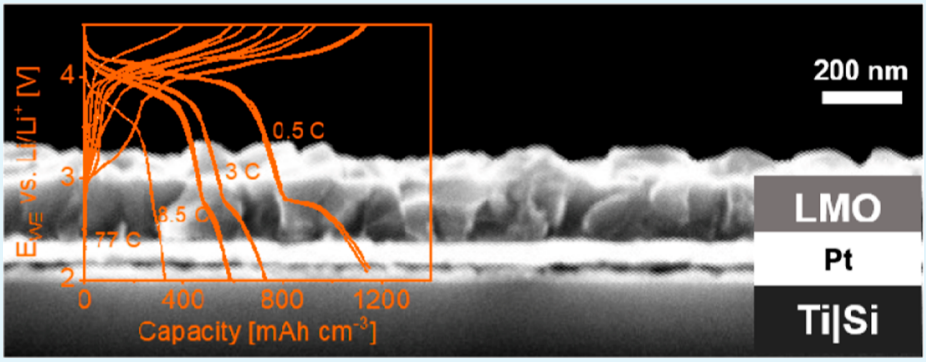

ABSTRACT: Extending the potential window toward the 3 V plateau below the typically used range could boost the effective capacity of $LiMn_2O_4$ spinel cathodes. This usually leads to an "overdischarge" of the cathode, which can cause severe material damage due to manganese dissolution into the electrolyte and a critical volume expansion (induced by Jahn−Teller distortions). As those factors determine the stability and cycling lifetime for all-solid-state batteries, the operational window of $LiMn_2O_4$ is usually limited to 3.5−4.5 V versus Li/Li^+ in common battery cells. However, it has been reported that nano-shaped particles and thin films can potentially mitigate these detrimental effects. We demonstrate here that porous $LiMn_2O_4$ thin-film cathodes with a certain level of off-stoichiometry show improved cycling stability for the extended cycling range of 2.0−4.5 V versus Li/Li^+. We argue through *operando* spectroscopic ellipsometry that the origin of this stability lies in the surprisingly small volume change in the layer during lithiation.

KEYWORDS: *spinel $LiMn_2O_4$, overdischarge, thin films, pulsed laser deposition, lithium-ion microbatteries, nanostructures*

1. INTRODUCTION

The growing importance of light-weighted, self-powered portable electronics (i.e., smartphones, tablets, microsensors, medical implants, and so on) in our everyday lives imposes demanding characteristics on the energy storage capacity and charging rate while maintaining high stability and safety of those devices. The need for miniaturized power sources with minimal volumetric footprint and high enough active material loading to provide energy to low-power electronics is steadily increasing, driven by the deployment of the internet of Things.[1] All-solid-state batteries are a well-positioned technology capable of maximizing volumetric energy densities, thus leading to high-performance micropower sources.[2,3] In particular, thin films (TFs) enable fast rates and low internal resistance while creating complex structures with a small area footprint, including three-dimensional (3D) designs.[4,5] One of the main issues with employing TFs is their small storage capacity. However, the obvious solution of using thicker films is not sufficient since thicker electrodes slow down the charge−discharge kinetics due to mass-diffusion limitations.[6] A second main issue is related to the critical volume changes in all-solid-state batteries and microbatteries, which can lead to severe interfacial strain, cracking, and loss of contact between the solid components.[7]

One popular cathode material in TFs is spinel lithium manganese oxide (LMO), known for its low cost, high rate capability, good cyclability, high voltage, and low toxicity.[8−11] Manganese ions are present in a mixed-valence state of $Mn^{3+/4+}$ for pristine $LiMn_2O_4$. During charge under cathodic currents,

Received: June 17, 2022
Accepted: June 28, 2022
Published: July 13, 2022

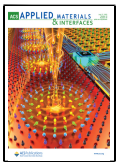

https://doi.org/10.1021/acsami.2c10798
ACS Appl. Mater. Interfaces 2022, 14, 33438−33446

one Li^+ ion is extracted, creating λ-MnO_2 and transforming all Mn^{3+} to Mn^{4+}, as described in eq S1 (see Supporting Information). In this commonly applied potential window between 3.5 and 4.5 V versus Li/Li^+ (4 V plateau), energy is stored with a high specific capacity of 595 mA h cm^{-3} (148 mA h g^{-1}, ρ = 4.02 g cm^{-3}). Theoretically, LMO is capable of reaching higher values in specific capacity with 1240 mA h cm^{-3} (296 mA h g^{-1}, ρ = 4.19 g cm^{-3}) when transforming all Mn^{4+} to Mn^{3+} in the anodic discharge down to ~2 V versus Li/Li^+ (3 V plateau) following the reaction in Equation S2.[11] The acceptance of an additional Li^+ ion in the LMO lattice forms $Li_2Mn_2O_4$, causing Mn-dissolution and an unwanted volume expansion (>5%) due to a more severe Jahn−Teller distortion. This process, known as "overdischarge", has been limiting the exploitation of the additional energy storage capacity associated with the 3 V plateau, thus avoiding the extension of the operational window toward 2.0−4.5 V versus Li/Li^+.[12]

Different strategies for the stabilization of the 3 V plateau have been pursued, such as nano-structuration, particle coating, introducing dopants, or dual-phase integration.[13] A controversial discussion of whether overdischarge may be endurable for LMO nano-sized samples is ongoing in the community. Kosilov et al.[12] predicted that micro-sized materials would result in enhanced stability. Conversely, Put et al.,[11] could demonstrate very thin LMO layers of 25 nm to have good capacity retention of 80% at 50 C with high specific capacities of 1240 mA h cm^{-3}. Very recently, an electrolyte- and salt-dependent SEI formation on top of LMO films has been suggested by De Taeye et al.[14] to impact the achievable capacities and the shape of the current−potential characteristics.

Sputtering[11,15] or pulsed laser deposition (PLD)[16,17,23] prevailed as commonly applied LMO TF fabrication techniques among other physical vapor depositions (PVD).[10] The collective concern across all techniques of Li-deficiency (highly volatile) is often counteracted with an overlithiation of the ceramic targets.[18,19] A more adaptable strategy to control the phase composition relies on the introduction of Li-rich targets (i.e., Li_2O and Li_3N) in the deposition sequence (e.g., multi-layering or co-deposition), which enjoys increasing popularity in the field of TFs.[3,20−24] This strategy enables the fabrication of complex compositional landscapes for the stabilization of the battery performance, such as dual-phases[25] and nanocomposites.[26] The first successful applications in the energy community[27] and Li-ion batteries[28] place greater attention on plural-phase nanocomposite structures and their beneficial stability for long-term applications.

In this work, LMO TFs deposited by a semi-industrial large-area (LA) PLD (scalable up to 4″ wafers) are studied for the first time toward the expansion of the operational potential window to 2.0−4.5 V versus Li/Li^+. A deeper understanding of the complex Li−Mn−O compositional landscape is provided for the lithiation/delithiation during overdischarge, and the real-time state-of-charge (SOC) is followed by spectroscopic ellipsometry (SE). *Operando* SE has only recently proven to be a powerful technique in monitoring real-time changes in optical transitions[29] and holds generally broad acceptance in determining TF and material properties.[30]

2. MATERIALS AND METHODS

2.1. Thin-Film Fabrication. Ceramic targets for TF depositions in the PLD are commercially available from Neyco for $LiMn_2O_4$ (99.9%) and from Codex for Li_2O (99.9%). Films were deposited on 80 nm Pt-coated Si chips (1 × 1 cm), where Pt acts as a back-side current collector and diffusion barrier, provided by the Institute of Microelectronics of Barcelona (IMB-CNM). Specifically, these substrates consist of $Si_{(100)}$-chips, coated with SiO_2 (100 nm), Si_3N_4 (300 nm), Ti (10 nm) adhesion layer, and Pt (80 nm) as the current collector. Cathode TFs are deposited in a LA PLD-5000 system from PVD products using a Coherent (Lambda Physik) COMPex Pro 205 KrF excimer laser (λ = 248 nm). LMO and Li_2O targets were ablated in a sequential manner following a multi-layer approach.[21] The reader is referred to Supporting Information, Figure S1 for further details. The multi-layer sequence consisted of a fixed ratio of ablation pulses of 4:3 between LMO (800 pulses per cycle) and Li_2O (600 pulses per cycle). This sequence was repeated for several cycles until the targeted film thickness of 320 nm or 200 nm was reached. All the depositions were carried out at a constant O_2 pressure of 20 mTorr at 650 °C. The substrate−target distance was kept at 90 mm with constant rotation. Laser fluence was set to 1.3 J cm^{-2} inside of the chamber.

2.2. Structural Characterization. Scanning electron microscopy (SEM) images were acquired with a Zeiss Auriga (30 kV Gemini FESEM column and an in-lens detector). X-ray diffraction was performed on an XRD Bruker-D8 Advance in theta−2theta configuration between 10 and 39° (step size of 0.01°). Raman spectroscopy was performed on an iHR320 spectrometer from HORIBA Scientific with a green laser (λ = 532 nm). Variable energy positron annihilation lifetime spectroscopy (VEPALS) measurements were conducted at the mono-energetic positron source (MePS) beamline at HZDR, Germany,[31] using a digital lifetime $CrBr_3$ scintillator detector coupled to a Hamamatsu R13089-100 PMT with a μ-metal shield and housed inside a solid Au casing with homemade software, employing a SPDevices ADQ14DC-2X digitizer with a 14-bit vertical resolution and a 2GS/s horizontal resolution[32] and with a time resolution function down to about 0.230 ns. The resolution function required for spectrum analysis uses two Gaussian functions with distinct intensities and shifts depending on the positron implantation energy, E_p. All spectra contained at least 1 × 10^7 counts. The typical lifetime spectrum $N(t)$ is described by $N(t) = \Sigma_i(1/\tau_i)\ I_i \exp(-t/\tau_i)$, where τ_i and I_i are the positron lifetime and intensity of the i-th component, respectively ($\Sigma I_i = 1$). All the spectra were deconvoluted using the non-linear least-square-based package PALSfit fitting software[33] into five discrete lifetime components, which directly evidence localized annihilation at two different defect types (sizes; τ_1 and τ_2), that is, small vacancy-like defects and their agglomerations. The third and fourth lifetime components (τ3 and τ4) represent two-pore populations of diameters d3 and d4. The fifth component (not shown) is residual and originates from ortho-positronium annihilation in vacuum and pore networks. The positron lifetime and its intensity have been probed as a function of positron implantation energy E_p or, in other words, implantation depth (thickness). Positrons have been accelerated and monoenergetically implanted into samples in the range between E_p = 1−12 keV, which realizes depth profiling. A mean positron implantation depth was approximated using a simple material density (ρ = 4.02 g·cm^{-3})-dependent formula: $\langle z \rangle = 36/\rho \cdot E_p^{1.62}$.[34] The average positron lifetime τ_{av} is defined as $\tau_{av} = \sum_i \tau_i \cdot I_i$ and has a high sensitivity to the defect size (type).

2.3. Optical Characterization. Spectroscopic ellipsometry (SE) was performed on a UVISEL Plus ellipsometer from HORIBA Scientific. The incident beam angle was fixed at 70° with a beam spot size of 2 mm^2. The optical data have been fitted with the DeltaPsi2 software using 1 Tauc−Lorentz and 1 Lorentz oscillator (see Equations S5 and S6). The $LiPF_6$ electrolyte is introduced in the model, following the porosity emulated by a mixed top layer using the effective medium approximation. The optical constant of the $LiPF_6$ is taken from the literature.[35] For the real-time probing of lithium (de-) intercalation, *operando* SE was performed inside an air-tight in situ chamber printed at IREC facilities with a Prusa i3 style 3D printer using photopolymer resin based on methacrylate. This air-tight chamber served as the three-electrode electrochemical cell that was assembled in an Ar-filled glovebox, sealed, and taken outside to the SE station. Electrochemical measurements were performed with a

https://doi.org/10.1021/acsami.2c10798
ACS Appl. Mater. Interfaces 2022, 14, 33438−33446

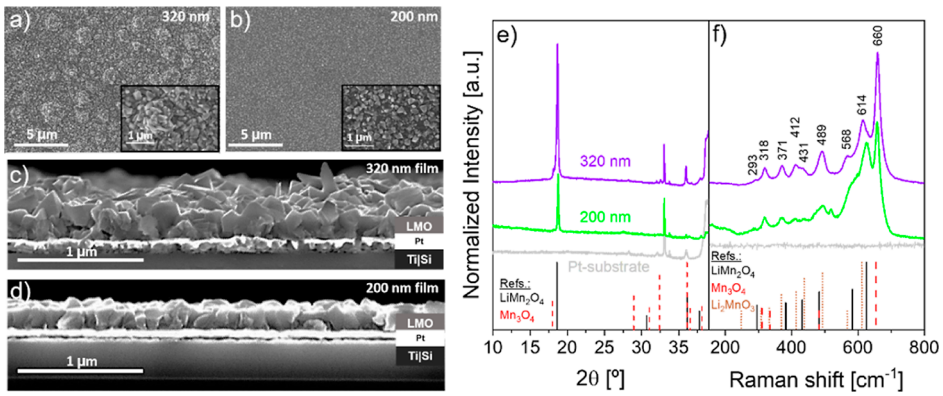

Figure 1. SEM images of LMO TFs fabricated by PLD top-view (a,c) and across-plane (b,d). The white scale bar corresponds to 1 μm. XRD patterns of polycrystalline LMO and Li_2O multi-layers for different thicknesses in (e), with the reference pattern from the bare Pt-substrate below for comparison (gray line). JCPDS references are shown for $LiMn_2O_4$ (00-035-0782) and Mn_3O_4 (01-080-0382). The corresponding Raman spectra in (f) are referenced in the literature for $LiMn_2O_4$, Mn_3O_4, and Li_2MnO_3.[36,37]

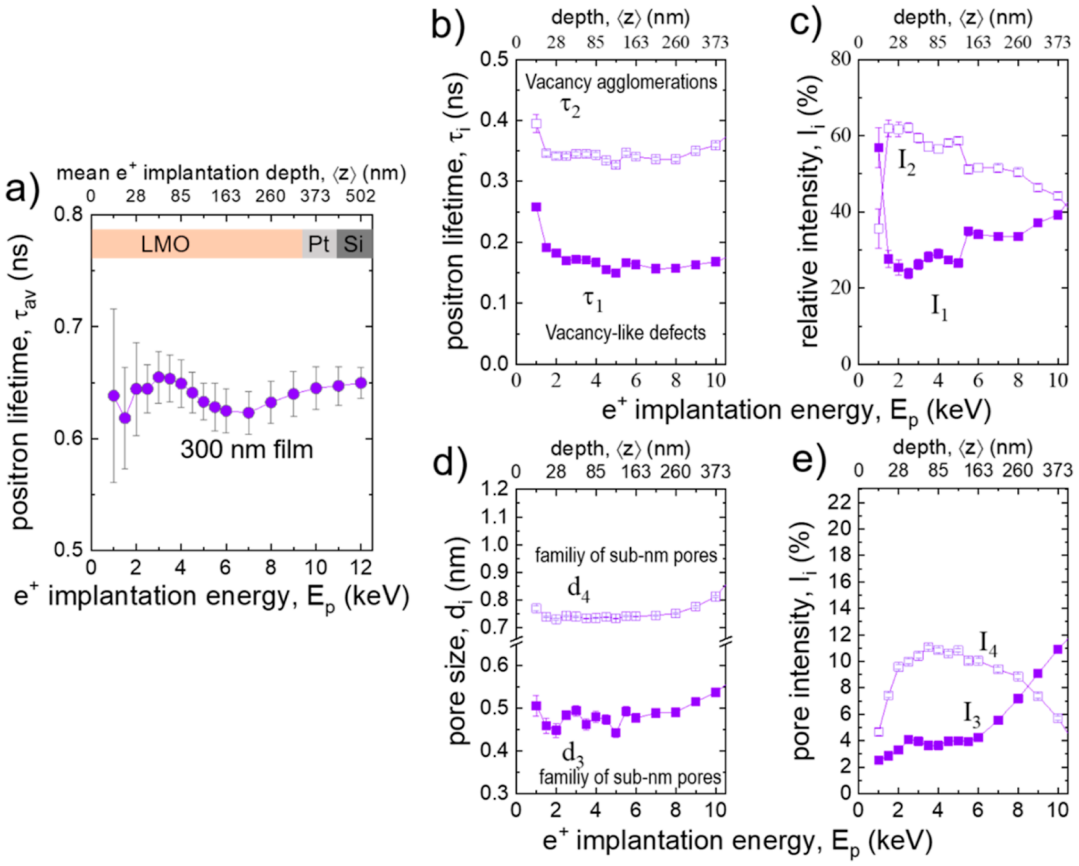

Figure 2. Average positron lifetime (a), τ_{av} indicates a weighted average of the defect size across film thickness. Detected defects are listed below the panel. Depth profiles of positron lifetimes (b) and relative intensities (c) for defects τ_1 and τ_2, corresponding to small vacancy-like defects and their agglomerations, respectively. Depth profiles of pore diameters recalculated from positron lifetimes (d) and their relative intensities (e) for defects τ_3 and τ_4, corresponding to two families of sub-nm small pores, respectively.

Biologic SP-50 (Lambda System) potentiostat. The acquisition time for the optical spectra collected for *operando* SE measurements was 1 s.

2.4. Electrochemical Analysis. For the electrochemical measurements, the LMO films were electrically contacted on the exposed Pt at the edges of the sample and embedded in a robust dual-component resin. In the electrochemical cell, the films were introduced as working electrodes and metallic lithium as counter and reference electrodes. The electrolyte employed was of 1 M LiPF6 EC/DMC = 50/50 (v/v) battery grade (Sigma-Aldrich).

3. RESULTS AND DISCUSSION

3.1. Structure and Microstructure of LMO. LMO TFs have been deposited by PLD using LMO and Li_2O targets in a multi-layer approach (see Supporting Information Figure S1). In Figure 1 the microstructure of the as-deposited LMO TF is presented as observed by SEM imaging.

A relatively rough surface and high porosity for the 320 nm thick films are obtained at moderate deposition temperatures of 650 °C. On the contrary, LMO films of 200 nm thickness

https://doi.org/10.1021/acsami.2c10798
ACS Appl. Mater. Interfaces 2022, 14, 33438−33446

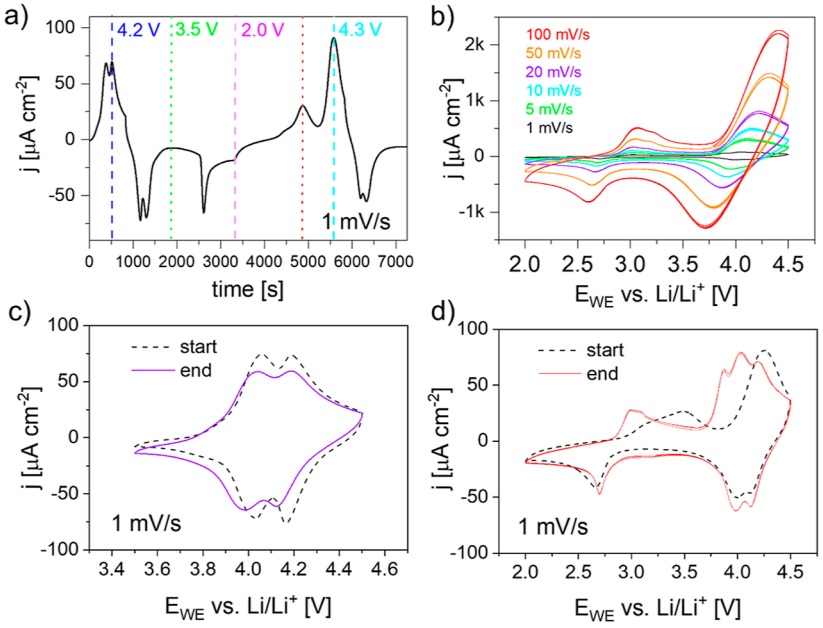

Figure 3. Cyclic voltammograms transitioning from the 4 V plateau to the 3 V plateau in (a). Significant changes in the apparent redox couples are marked at the corresponding potential by vertical dashed lines. Cyclic voltammograms at increasing scan rates in the extended range are collected in (b). Comparison of cyclic voltammograms of the LMO films between the initial (dashed lines) and the final (solid lines) measurements in the restricted (c) and extended (d) ranges. The film was cycled for more than 24 h at different scan rates in the extended range in between the first and last measurements.

show better film homogeneity in particle size with a smoother surface and grains with non-preferential orientation, illustrating their polycrystalline nature.

Structural analysis is provided in Figure 1 with XRD (e) and Raman (f) analysis. Both TF samples show the presence of spinel $LiMn_2O_4$ as the main phase. While the XRD pattern of the 200 nm film is dominated by the (111) reflection of LMO with no other detectable parasitic phases, the 300 nm film shows small quantities of Mn_3O_4. This is further exemplified by Raman spectroscopy, where the spectra show subtle differences compared to the pure LMO spinel. First, the absorption band at c.a. 620 cm^{-1} can be ascribed to the A_{1g} mode of $LiMn_2O_4$. However, it appears slightly shifted toward lower energies compared to the expected values (between 623 and 626 cm^{-1}).[38] This small shift has been observed experimentally in $LiMn_2O_4$ with significant concentrations of crystalline defects, especially Li and Mn vacancies, and has been attributed to an increase in the Mn−O bond length.[39] This is not surprising since cation-deficient structures are typically observed in PLD-deposited layers.[40] This fact could also explain the intense peak around 660 cm^{-1}, which is not allowed for ideal spinel structures but has been shown to be activated when symmetry is reduced due to defects.[39] Alternatively, it is also probable that this band appears as a consequence of the presence of the Mn_3O_4 phase with a Raman shift at 653 cm^{-1}.[41,42] The rest of the lower-intensity peaks at 293, 318, 371, 412, 431, and 489 cm^{-1} have been reported for Li-rich spinels.[37] The origin of the observed slight non-stoichiometric material distribution might be related to the layer-by-layer deposition process, the complex landscape of Mn oxidation states, the loss of volatile lithium, and a reducing atmosphere during deposition, overall leading to both Li-rich domains and regions with cation deficiencies.

To shed some light on these cation deficiencies and other sub-nm defects, we performed VEPALS measurements on the 300 nm LMO film (Figure 2). In VEPALS, the films are irradiated with positrons that recombine (annihilate) with electrons in the films at defined depths, creating gamma rays, which are subsequently detected. The measurement of the positron lifetime provides direct information on the type of negatively-charged and neutral defects and their concentration. In Figure 2a, the positron lifetime versus positron implantation energy E_p (thickness) shows a rather homogeneous value across the entire thickness, with a slight decrease in the average lifetime as positrons penetrate deeper into the film. This means that the average defect size decreases from the surface toward the substrate. The deconvolution of the spectra (see Experimental Section 2.2) showed four main types of defects: on one hand, small vacancy-like defects and their agglomerations (lifetime components τ_1 and τ_2 and their relative intensities I_1 and I_2, respectively, Figure 2b,c). On the other hand, two families of sub-nm pores (micropores with spherical sizes $d_3 \approx 0.47$ nm and $d_4 \approx 0.75$ nm) and intensities I_3 and I_4, respectively, Figure 2d,e). The pore size was calculated using the Wada and Hyodo shape-free model.[43] Overall, both pore families and vacancy-related defects exhibit a homogeneous distribution across the thickness of the film. Comparing the relative intensities, one can see that the vacancy-related defects dominate the average lifetime of the positrons ($I_1 + I_2 > I_3 + I_4$), indicating the larger presence of vacancies in the film. All in all, these PALS measurements demonstrate the presence of cationic defects and pores on our films and can potentially play a role in suppressing and/or alleviating the Jahn−Teller distorsions.[44]

3.2. Electrochemical Characterization of the Full Potential Window. Representative first cyclic voltammograms are exemplified for the 320 nm thick films in the "safe" potential range of 3.5−4.5 V versus Li/Li^+ (discussed later on) in 1 M $LiPF_6$ with the EC/DMC (1:1) electrolyte in an Ar-filled glovebox. In a subsequent step, the operational window is

https://doi.org/10.1021/acsami.2c10798
ACS Appl. Mater. Interfaces 2022, 14, 33438−33446

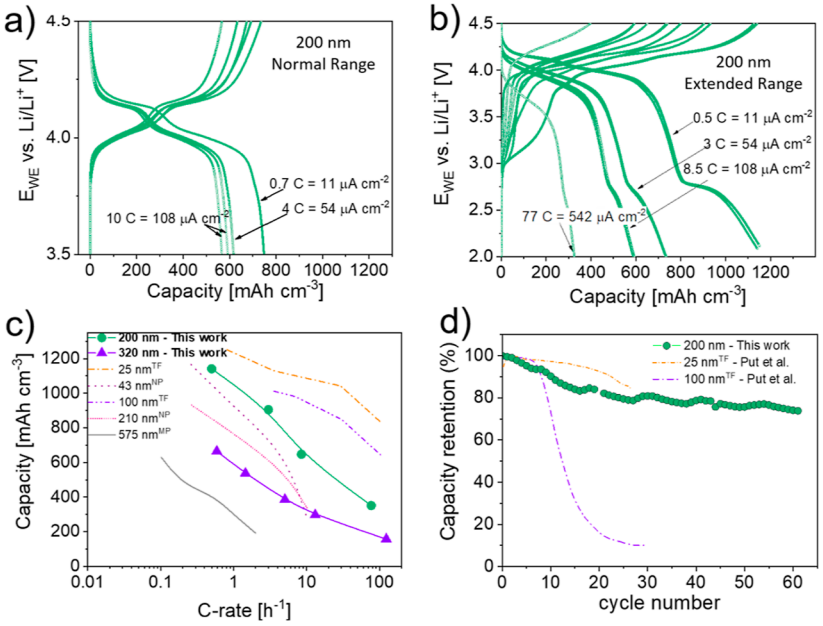

Figure 4. Charge (cathodic) and discharge (anodic) curves of different C-rates for a LMO layer of 200 nm thickness are shown including the 4 V plateau (a) and the extended potential range including the 3 V plateau (b). Resulting volumetric discharge capacities for the full potential range of 320 nm (triangles) and 200 nm (circles) thick LMO films are plotted over the C-rate (logarithmic scale) in (c). Reference is made to RF-sputtered LMO TF,[11] LMO nanoparticles,[52] and microparticles in a thick layer.[51] Capacity retention evaluated under long-term cycling of the 200 nm thick layer in the full potential window between 2.0 and 4.5 V versus Li/Li^+ for 60 cycles at 10 $\mu A\ cm^{-2}$ (0.8 C) (d) and its comparison to RF-sputtered LMO TFs.[11]

extended down to 2.0 V versus Li/Li^+, including the 3 V plateau in Figure 3a at 1 mV s^{-1} scan rate.

The expected redox peaks for the $Mn^{3+/4+}$ transition (see Equation S1) around 4.2 V are well defined and fully reversible in the 4 V plateau. For passing to the 3 V plateau, an anodic discharge current is applied beyond 3.5 V and an additional Li^+ is intercalated (see Equation S2). A strong anodic reduction peak appears at 2.7 V related to the full transition of mixed-valence $Mn^{3+/4+}$ to Mn^{3+} under the formation of tetragonal $Li_2Mn_2O_4$. The scan is reversed at 2 V with a cathodic current for Li^+ extraction (charging), leading to the structural transition of tetragonal-to-spinel around 3.5 V. With further potential increase up to 4.5 V, the oxidation peak of the $Mn^{3+/4+}$ transition forms one joint redox peak around 4.3 V instead of separating into the usual, well-defined doublet oxidation peaks. With increasing cycle numbers and scan rates, the redox peaks are symmetric single-peaks for both cathodic and anodic currents as demonstrated in Figure 3b. Similar behavior has been reported by Rougier et al.,[45] who assigned the joint redox peak to the additional obstacles to be overcome for lithium (de-) intercalation, such as lattice distortion (see Figure S2) and the disproportionation reaction of manganese Mn^{3+} described in Equation S3 (see Supporting Information) and by De Taeye and Vereecken,[14] who observed the formation of an SEI rich in P and F, limiting the insertion kinetics.

Figure 3c demonstrates the effect of peak broadening in the 4 V plateau being vanished when restricted again to the typical high-voltage region between 3.5 and 4.5 V versus Li/Li^+, showing the classic double oxidation peak anew. While the limited range between 3.5 and 4.5 V versus Li/Li^+ shows slightly damped redox peaks when comparing the CV from the beginning (start) to the end, the voltammogram including the 3 V plateau also shows improved redox peak definition and an additional oxidation peak at 3.8 V, which is ascribed in literature to parasitic reactions taking place.[11,46−50]

In Figure 4 the volumetric specific capacities obtained at various C-rates are examined for the first charge and discharge cycles in the 4 V plateau (a) and then for the extended range, including the 3 V plateau (b). Starting with low C-rates < 1 C, both potential regions in Figure 4a,b demonstrate exceptionally high discharge capacities of 750 mA h cm^{-3} at 3.5 V versus Li/Li^+ and 1150 mA h cm^{-3} at 2.1 V versus Li/Li^+. With increasing C-rate, the volumetric specific capacities decrease and slower reaction kinetics become evident for the full potential window of LMO, dealing with lattice distortion and more complex defect chemistries. As with C-rates ≥ 3 C, there is merely an advantage in specific capacity compared to the restrained potential region of the 4 V plateau. The superior energy density is restrained by the loss in high rate capability. The resulting volumetric specific capacities at different C-rates for 320 nm and 200 nm thick films are compared in Figure 4c with sputtered LMO TFs and micro- and nano-sized samples. The dependence of the volumetric specific capacity on the C-rate follows a clear trend, being highly dependent on the particle size or film thickness, and therefore appears strongly correlated to the difference in diffusion path lengths. The lowest capacities are reached when cycling microparticles are packed in a 575 nm thick layer in the full potential region of LMO,[51] whereas sputtered TFs of 25 nm in thickness show the highest capacities and exhibit very fast reaction kinetics.[11] One reason for this behavior is the change in lithiation mechanism from micro- to nano-shaped materials at a critical particle size. $Li_{1+x}Mn_2O_4$ bulk-type materials tend to react in a "core−shell" manner when lithiating, forming a Li-rich outer layer around the micro-particles. Nano-shapes below 100 nm rather form solid solutions, leading to fewer obstacles in the diffusion process. This seems to be applicable in our case, given the

https://doi.org/10.1021/acsami.2c10798
ACS Appl. Mater. Interfaces 2022, 14, 33438−33446

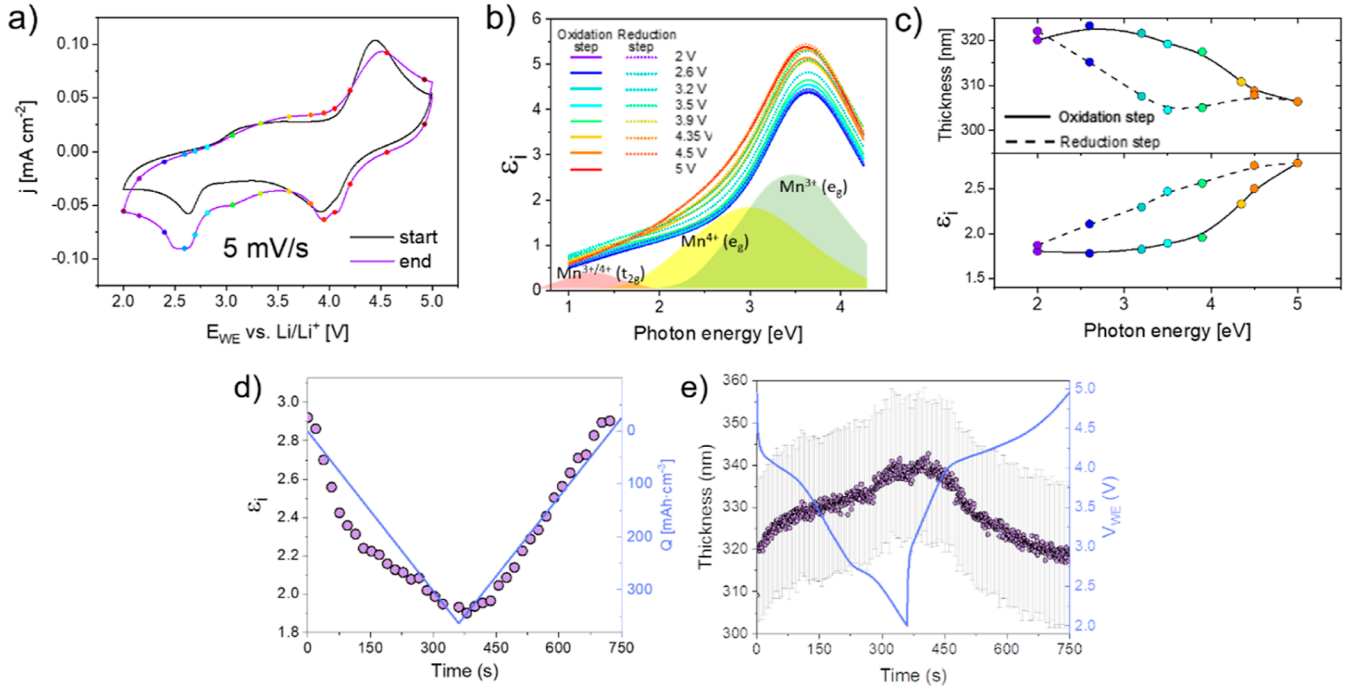

Figure 5. a) Cyclic voltammetry of LMO cathode TFs between 2.0 and 5.0 V versus Li/Li$^+$ in 1 M $LiPF_6$ EC/DMC (1:1) collected in an air-tight, 3D-printed optical chamber at a 5 mV s^{-1} scan rate. CV is shown before (start) and after (end) the *operando* monitoring by SE. Voltage instants for the SE spectra are indicated as circles with the color of the corresponding voltage. The related change in optical absorption ε_i of $Mn^{3+/4+}$ is shown in (b). The evolution of ε_i at 2.8 eV is an indicator of the SOC and is depicted in (c) for different voltages. The normalized change of ε_i at 2.8 eV during galvanostatic delithiation at 9.5 C is shown in (d) and the corresponding change in the (total) thickness upon lithium extraction in (e) for both the same *C*-rate and accumulated charge.

presence of a slight slope in the 4 V plateau, deviating from the canonical flat shape expected for a two-phase reaction mechanism. Despite the high surface-to-volume ratio, the formation of the solid solution for Li-rich and -poor states eliminates separated domains and hence facilitates mass transfer, allowing the intercalation of up to 2.5 Li^+ resulting in $Li_{2.5}Mn_2O_4$.[52] This causes a clear increase in specific capacities at high C-rates for nano-sized materials in Figure 4c, whereas thicker layers with greater spatial dimensions in their crystallites behave similarly to bulk-type materials. Our work shows that LMO TFs deposited by LA-PLD follow this trend and position the volumetric specific capacities of 320 nm thick films between the micro- and nanoparticles. Thinner layers with 200 nm (Figure 4c) exhibit higher specific capacities in the full potential range, supporting the previously observed correlation of film thickness and capacity of RF-sputtered LMO TFs by Put et al.[11] The remarkable increase in thickness when compared to literature results in potential total capacities of ∼18 μA h·cm^{-2} (see Supporting Information for comparison with literature). Nonetheless, the limited cycling stability due to volume expansion, cracking, loss of contact with the current collector, Mn-dissolution, and so forth are dissuading factors for the exploration of LMO in its full potential range. To evaluate the stability of the LMO TFs presented in this work, 200 nm thick films have been subjected to long-term cycling at a C-rate of 0.8 C in Figure 4d.

60 charge−discharge cycles have been repeated in the potential range of 2.0−4.5 V versus Li/Li$^+$ and are compared with the capacity retention of RF-sputtered layers (25 and 100 nm thickness) cycled in the same potential window at 1 C, showing a capacity drop of only about 26% while cycling at 0.8 C for 60 cycles. This degradation, while relevant, is still much smaller than the one observed in the literature.[11,51] Compared to RF-sputtered TFs of 100 nm thickness, capacity decays much faster when cycled at 1 C. After 25 cycles, only ∼15% of the initial capacity is still accessible. Thinner layers, in comparison, lose less capacity per cycle more gradually, with only ∼11% decrease in specific capacity after 25 cycles. All in all, 200 nm thick LMO TFs deposited by multi-layer PLD show good capacity retention of 74% when performing 60 cycles at 0.8 C. In the following, real-time *operando* SE aims to provide deeper insights into the reasons for improved cycling stability.

3.3. Study of Cathode Evolution along with the Extended Range by Operando SE. The change in optical characteristics of LMO during charge/discharge is monitored by *operando* SE for the first time in a wide electrochemical potential window between 2.0 and 5.0 V versus Li/Li$^+$. The measurement setup is assembled under a protective Ar-atmosphere (see details in the Experimental Section) and transferred to the ambient atmosphere in an air-tight optical chamber. Figure 5a presents the cyclic voltammograms obtained inside the liquid cell, which are in accordance with the ones presented in Figure 3b,d and show good reversibility of significant redox peaks over the full potential range. Colored points in the CV represent the voltage instants at which optical spectra were obtained by using SE acquisition. The imaginary part of the permittivity ε_i, directly linked with optical absorption, is shown in Figure 5b. It was obtained from the complex dielectric function (Equation S4) under the application of a model containing two Lorentz oscillators (see details in the Supporting Information).

Consistent with the results reported in previous studies of $LiMn_2O_4$ films, we observe a broad absorption band centered

https://doi.org/10.1021/acsami.2c10798
ACS Appl. Mater. Interfaces 2022, 14, 33438−33446

around 2.8−3.3 eV, attributed to the electronic transitions between O^{2-} (2p) and Mn^{4+} (e_g), and a second absorption band between 3.4 and 4.0 eV, correlated to O^{2-} (2p)−Mn^{3+} (e_g) transitions. A small contribution is also observed at low energies, which has been ascribed to $Mn^{3+}/^{4+}$ (t_{2g}) interband transitions. Due to the limited spectral range imposed by the absorption of the electrolyte, mostly the absorption at around 3.0 eV will determine the thickness of the LMO layer. Figure 5c shows the evolution of ε_i at 2.8 eV (bottom) and the thickness variation along with the CV (top). A certain hysteresis in the closed-loop experiments is found. This is an indication that, while being at the same potential, the equilibrium reached by the layer is different during lithiation and delithiation through the voltage sweep at 5 mV s^{-1}.

To investigate the changes in the optical properties and the thickness of the layer during lithium (de-) intercalation more accurately, a continuous *operando* SE experiment was performed, with a sampling rate of 1s, while a galvanostatic sweep rate is applied under a current of 10 μA. The sample is fully delithiated before the experiment. When the lower imposed voltage limit of 2.0 V is reached, the current is reversed, and the sample is again oxidized until the voltage rises to 5.0 V. All the acquired spectra are fitted using the previously defined model and simplified by fixing the top layer thickness and porosity to reduce the number of uncertainties. Also, only two absorption bands are considered. The first is represented using a broad Lorentz oscillator and takes into account the variation in the absorption in the intermediate range (2.0−3.5 eV). The second one accounts for the absorption at higher energies, centered at around 4.0−5.0 eV (out of the experimental observable range). In this way, the layer permittivity is obtained in the acquisition spectral range, and the volume changes will be known by the variation of the dense bottom layer thickness. The optical absorption extracted at 2.8 eV in Figure 5d is expected to follow the Li (de-) insertion in the layer, providing an indicator of the state-of-charge along the complete cycle.[29] While this is clearly the case for the delithiation sweep, there are some deviations during the first lithiation which could be attributed to the investment of the introduced current in the generation of an SEI or some other process not related to the TF reduction.[14]

Interestingly, it is also possible to accurately infer the thickness variation along the galvanostatic sweep, Figure 5e. Not surprisingly, the volume of the $Li_xMn_2O_4$ layer increases as lithium is inserted. A small (and expected) thickness enhancement of c.a. 2.5% takes place during 8a site occupancy in the high-voltage intercalation plateau ($0 < x < 1$), where the cubic structure is known to be maintained. In the low-voltage intercalation range ($1 < x < 2$), the volume changes are slightly more pronounced (c.a. 3%). However, a much larger expansion (of 5.6%) would be expected since the lithium insertion in this plateau involves the filling of octahedral 16c sites, which is accompanied by a large volume change.[53] The relatively small variation observed in this work might be explained by the presence of defects in the deposited layer. Taking into account the nature of the multi-layer PLD deposition procedure described in Section S1, it is likely to have slight variations in the pursued stoichiometry. Indeed, Song et al. reported very small volume changes in $Li_{1+\delta}Mn_2O_4$, which was associated with the presence of a tetragonal-spinel structure.[54] Van Der Ven et al. also provided other possible explanations for the reduced volume change in defective $LiMn_2O_4$.[55] Their calculations showed that the main reason for the volume expansion comes from the filling of the e_g level when an electron is added to reduce Mn^{4+} to Mn^{3+}. While the t_{2g} can be considered as non-bonding, the e_g level is anti-bonding of the Mn (d) and O (p) orbitals. For this reason, its filling might produce a Mn−O elongation and is considered the main cause of volume change above Jahn−Teller distortion or the introduction of Li in the material. They hypothesized that a Mn−O bond compression could influence the crystal field splitting in such a way that the first lowest spin t_{2g} level becomes lower in energy than the first up-spin e_g level, reducing the impact of the bond length variation. Moreover, the Raman signal of the layers and the PALS measurements, as discussed before in Section 2.1, indicate a reduction of the expected Mn−O bond and the presence of cation deficiencies and pores that are compatible with this hypothesis, which could be behind the remarkably higher tolerance to cycling presented by our layers, which is in agreement with recent studies.[44]

4. CONCLUSIONS

The electrochemical stability of LMO TFs, deposited by multi-layering in the PLD, has been studied in an organic electrolyte across the so-called "overdischarge" regime of the material. The layers have been subjected to different C-rates in the full potential stability window of 2.0−4.5 V versus Li/Li^+, demonstrating very high discharge capacities of 1150 mA h cm^{-3} at 0.5 C. This is a massive improvement when comparing the discharge capacity of the same film reached in the commonly applied potential range of 3.5−4.5 V versus Li/Li^+ with a discharge capacity of 750 mA h cm^{-3} at 0.7 C. The layers could maintain 74% of the initial capacity after 60 cycles at a *C*-rate of 0.8 C, which can be considered a promising result in comparison to literature as no additional doping or protective layer was necessary. *Operando* SE carried out in the whole range of applied potential revealed that only small volume changes take place in the layer while providing accurate monitoring of the SOC. The good cycling stability may be the consequence of these very small volume changes, possibly resulting from the presence of defects and the off-stoichiometry of the deposited layers as observed by PALS. Our work suggests that defect engineering can potentially enable the use of LMO as an efficient TF cathode in micro-power sources.

■ ASSOCIATED CONTENT

Supporting Information

The Supporting Information is available free of charge at https://pubs.acs.org/doi/10.1021/acsami.2c10798.

Schematics and details regarding the thin-film depositions by pulsed laser deposition, the electrochemical properties of $LiMn_2O_4$, and the derivation of the optical properties through SE (PDF)

■ AUTHOR INFORMATION

Corresponding Authors

Alex Morata − *Catalonia Institute for Energy Research (IREC), Barcelona 08930, Spain;* orcid.org/0000-0002-3300-4636; Email: amorata@irec.cat

Albert Tarancón − *Catalonia Institute for Energy Research (IREC), Barcelona 08930, Spain; Catalan Institution for Research and Advanced Studies (ICREA), Barcelona 08010,*

Spain; orcid.org/0000-0002-1933-2406;
Email: atarancon@irec.cat

Authors

Valerie Siller − *Catalonia Institute for Energy Research (IREC), Barcelona 08930, Spain;* Present Address: Valerie Siller: Paul Scherrer Institut, Forschungsstrasse 111, 5232 Villigen, Switzerland; orcid.org/0000-0001-5477-6304

Juan Carlos Gonzalez-Rosillo − *Catalonia Institute for Energy Research (IREC), Barcelona 08930, Spain;* orcid.org/0000-0001-6017-174X

Marc Nuñez Eroles − *Catalonia Institute for Energy Research (IREC), Barcelona 08930, Spain*

Federico Baiutti − *Catalonia Institute for Energy Research (IREC), Barcelona 08930, Spain;* orcid.org/0000-0001-9664-2486

Maciej Oskar Liedke − *Helmholtz-Zentrum Dresden—Rossendorf, Institute of Radiation Physics, Dresden 01328, Germany*

Maik Butterling − *Helmholtz-Zentrum Dresden—Rossendorf, Institute of Radiation Physics, Dresden 01328, Germany*

Ahmed G. Attallah − *Helmholtz-Zentrum Dresden—Rossendorf, Institute of Radiation Physics, Dresden 01328, Germany;* orcid.org/0000-0002-7759-0315

Eric Hirschmann − *Helmholtz-Zentrum Dresden—Rossendorf, Institute of Radiation Physics, Dresden 01328, Germany*

Andreas Wagner − *Helmholtz-Zentrum Dresden—Rossendorf, Institute of Radiation Physics, Dresden 01328, Germany*

Complete contact information is available at: https://pubs.acs.org/10.1021/acsami.2c10798

Notes

The authors declare no competing financial interest.

■ ACKNOWLEDGMENTS

This project has received funding from the European Union's Horizon 2020 research and innovation program under grant agreement no 824072 (HARVESTORE), from the European Regional Development Fund under the FEDER Catalonia Operative Programme 2014−2020 (FEM-IoT, 001-P-00166), and the "Generalitat de Catalunya" (2017 SGR 1421, NANOEN). J.C.G.R. acknowledges the financial support provided by the European Union's Horizon 2020 research and innovation program under the Marie Skłodowska-Curie grant agreement no. 801342 (Tecniospring INDUSTRY), as well as by the Agency for Business Competitiveness of the Government of Catalonia. SE measurements and models have been developed in collaboration with HORIBA France SAS. Parts of this research were carried out at ELBE at the Helmholtz-Zentrum Dresden - Rossendorf e. V., a member of the Helmholtz Association. We would like to thank the facility staff for their assistance.

■ REFERENCES

(1) Raj, A.; Steingart, D. Review-Power Sources for the Internet of Things. *J. Electrochem. Soc.* **2018**, *165*, B3130−B3136.

(2) Sun, C.; Liu, J.; Gong, Y.; Wilkinson, D. P.; Zhang, J. Recent Advances in All-Solid-State Rechargeable Lithium Batteries. *Nano Energy* **2017**, *33*, 363−386.

(3) Zhu, Y.; Gonzalez-Rosillo, J. C.; Balaish, M.; Hood, Z. D.; Kim, K. J.; Rupp, J. L. M. Lithium-Film Ceramics for Solid-State Lithionic Devices. *Nat. Rev. Mater.* **2021**, *6*, 313−331.

(4) Long, J. W.; Dunn, B.; Rolison, D. R.; White, H. S. 3D Architectures for Batteries and Electrodes. *Adv. Energy Mater.* **2020**, *10*, 2002457−20024576.

(5) Ashby, D. S.; Choi, C. S.; Edwards, M. A.; Talin, A. A.; White, H. S.; Dunn, B. S. High-Performance Solid-State Lithium-Ion Battery with Mixed 2D and 3D Electrodes. *ACS Appl. Energy Mater.* **2020**, *3*, 8402−8409.

(6) Moitzheim, S.; Put, B.; Vereecken, P. M. Advances in 3D Thin-Film Li-Ion Batteries. *Adv. Mater. Interfaces* **2019**, *6*, 1900805.

(7) Koerver, R.; Zhang, W.; De Biasi, L.; Schweidler, S.; Kondrakov, A. O.; Kolling, S.; Brezesinski, T.; Hartmann, P.; Zeier, W. G.; Janek, J. Chemo-mechanical expansion of lithium electrode materials - on the route to mechanically optimized all-solid-state batteries. *Energy Environ. Sci.* **2018**, *11*, 2142−2158.

(8) Thackeray, M. M.; Mansuetto, M. F.; Bates, J. B. Structural Stability of LiMn2O4 Electrodes for Lithium Batteries. *J. Power Sources* **1997**, *68*, 153−158.

(9) Sheth, J.; Karan, N. K.; Abraham, D. P.; Nguyen, C. C.; Lucht, B. L.; Sheldon, B. W.; Guduru, P. R. In Situ Stress Evolution in Li1+xMn2O4Thin Films during Electrochemical Cycling in Li-Ion Cells. *J. Electrochem. Soc.* **2016**, *163*, A2524−A2530.

(10) Liang, X.; Tan, F.; Wei, F.; Du, J. Research Progress of All Solid-State Thin Film Lithium Battery. *IOP Conf. Ser. Earth Environ. Sci.* **2019**, *218*, 012138.

(11) Put, B.; Vereecken, P. M.; Labyedh, N.; Sepulveda, A.; Huyghebaert, C.; Radu, I. P.; Stesmans, A. High Cycling Stability and Extreme Rate Performance in Nanoscaled LiMn2O4 Thin Films. *ACS Appl. Mater. Interfaces* **2015**, *7*, 22413−22420.

(12) Kosilov, V. V.; Potapenko, A. V.; Kirillov, S. A. Effect of Overdischarge (Overlithiation) on Electrochemical Properties of LiMn2O4 Samples of Different Origin. *J. Solid State Electrochem.* **2017**, *21*, 3269−3279.

(13) Armstrong, M. J.; O'Dwyer, C.; Macklin, W. J.; Holmes, J. D. Evaluating the Performance of Nanostructured Materials as Lithium-Ion Battery Electrodes. *Nano Res.* **2014**, *7*, 1−62 Tsinghua University Press January 4.

(14) De Taeye, L. L.; Vereecken, P. M. Detrimental MnPO4F and MnF2 formation on LiMn2O4 in the 3 V region. *J. Mater. Chem. A* **2021**, *9*, 23256−23268.

(15) Mürter, J.; Nowak, S.; Hadjixenophontos, E.; Joshi, Y.; Schmitz, G. Grain Boundary Transport in Sputter-Deposited Nanometric Thin Films of Lithium Manganese Oxide. *Nano Energy* **2018**, *43*, 340−350.

(16) Jamil, H.; Khaleeq-Ur-Rahman, M.; Dildar, I. M.; Shaukat, S. Structural and Optical Properties of Manganese Oxide Thin Films Deposited by Pulsed Laser Deposition at Different Substrate Temperatures. *Laser Phys.* **2017**, *27*, 096101.

(17) Julien, C. M.; Mauger, A. Pulsed Laser Deposited Films for Microbatteries. *Coatings* **2019**, *9*, 386.

(18) Simmen, F.; Lippert, T.; Novák, P.; Neuenschwander, B.; Döbeli, M.; Mallepell, M.; Wokaun, A. The influence of lithium excess in the target on the properties and compositions of Li1+x Mn2O4−δ thin films prepared by PLD. *Appl. Phys. A* **2008**, *93*, 711−716.

(19) Dumont, T.; Lippert, T.; Döbeli, M.; Grimmer, H.; Ufheil, J.; Novák, P.; Würsig, A.; Vogt, U.; Wokaun, A. Influence of experimental parameter on the Li-content of LiMn2O4 electrodes produced by pulsed laser deposition. *Appl. Surf. Sci.* **2006**, *252*, 4902−4906.

(20) Balaish, M.; Gonzalez-Rosillo, J. C.; Kim, K. J.; Zhu, Y.; Hood, Z. D.; Rupp, J. L. M. Processing Thin but Robust Electrolytes for Solid-State Batteries. *Nat. Energy* **2021**, *6*, 227−239.

(21) Fehse, M.; Trócoli, R.; Hernández, E.; Ventosa, E.; Sepúlveda, A.; Morata, A.; Tarancón, A. An Innovative Multi-Layer Pulsed Laser Deposition Approach for LiMn2O4 Thin Film Cathodes. *Thin Solid Films* **2018**, *648*, 108−112.

(22) Fehse, M.; Trócoli, R.; Ventosa, E.; Hernández, E.; Sepúlveda, A.; Morata, A.; Tarancón, A. Ultrafast Dischargeable LiMn2O4 Thin-

Film Electrodes with Pseudocapacitive Properties for Microbatteries. *ACS Appl. Mater. Interfaces* **2017**, *9*, 5295−5301.
(23) Pagani, F.; Döbeli, M.; Battaglia, C. Lithium-Ion Transport in Li 4 Ti 5 O 12 Epitaxial Thin Films vs. State of Charge. *Batteries Supercaps* **2021**, *4*, 316−321.
(24) Gonzalez-Rosillo, J. C.; Balaish, M.; Hood, Z. D.; Nadkarni, N.; Fraggedakis, D.; Kim, K. J.; Mullin, K. M.; Pfenninger, R.; Bazant, M. Z.; Rupp, J. L. M. Lithium-Battery Anode Gains Additional Functionality for Neuromorphic Computing through Metal-Insulator Phase Separation. *Adv. Mater.* **2020**, *32*, 1907465.
(25) Bhatti, H. S.; Anjum, D. H.; Ullah, S.; Ahmed, B.; Habib, A.; Karim, A.; Hasanain, S. K. Electrochemical Characteristics and Li+ Ion Intercalation Kinetics of Dual-Phase Li4ti5o12/Li2tio3 Composite in the Voltage Range 0-3 V. *J. Phys. Chem. C* **2016**, *120*, 9553−9561.
(26) Huang, J.; Li, W.; Yang, H.; MacManus-Driscoll, J. L. Tailoring Physical Functionalities of Complex Oxides by Vertically Aligned Nanocomposite Thin-Film Design. *MRS Bull.* **2021**, *46*, 159−167.
(27) Baiutti, F.; Chiabrera, F.; Acosta, M.; Diercks, D.; Parfitt, D.; Santiso, J.; Wang, X.; Cavallaro, A.; Morata, A.; Wang, H.; Chroneos, A.; MacManus-Driscoll, J.; Tarancon, A. A High-Entropy Manganite in an Ordered Nanocomposite for Long-Term Application in Solid Oxide Cells. *Nat. Commun.* **2021**, *12*, 2660.
(28) Cunha, D. M.; Huijben, M. Lithium-Based Vertically Aligned Nanocomposites for Three-Dimensional Solid-State Batteries. *MRS Bull.* **2021**, *46*, 152−158.
(29) Morata, A.; Siller, V.; Chiabrera, F.; Nuñez, M.; Trocoli, R.; Stchakovsky, M.; Tarancón, A. Operando probing of Li-insertion into LiMn2O4 cathodes by spectroscopic ellipsometry. *J. Mater. Chem. A* **2020**, *8*, 11538−11544.
(30) Losurdo, M.; Bergmair, M.; Bruno, G.; Cattelan, D.; Cobet, C.; de Martino, A.; Fleischer, K.; Dohcevic-Mitrovic, Z.; Esser, N.; Galliet, M.; others. Spectroscopic Ellipsometry and Polarimetry for Materials and Systems Analysis at the Nanometer Scale: State-of-the-Art, Potential, and Perspectives. *J. Nanopart. Res.* **2009**, *11*, 1521−1554.
(31) Wagner, A.; Butterling, M.; Liedke, M. O.; Potzger, K.; Krause-Rehberg, R. Positron Annihilation Lifetime and Doppler Broadening Spectroscopy at the ELBE Facility. *AIP Conf. Proc.* **2018**, *1970*, 040003.
(32) Hirschmann, E.; Butterling, M.; Hernandez Acosta, U.; Liedke, M. O.; Attallah, A. G.; Petring, P.; Görler, M.; Krause-Rehberg, R.; Wagner, A. A New System for Real-Time Data Acquisition and Pulse Parameterization for Digital Positron Annihilation Lifetime Spectrometers with High Repetition Rates. *J. Instrum.* **2021**, *16*, P08001.
(33) Olsen, J. V.; Kirkegaard, P.; Pedersen, N. J.; Eldrup, M. PALSfit: A new program for the evaluation of positron lifetime spectra. *Phys. Status Solidi* **2007**, *4*, 4004−4006.
(34) Dryzek, J.; Horodek, P. GEANT4 Simulation of Slow Positron Beam Implantation Profiles. *Nucl. Instrum. Methods Phys. Res., Sect. B* **2008**, *266*, 4000−4009.
(35) McArthur, M. A.; Trussler, S.; Dahn, J. R. In Situ Investigations of SEI Layer Growth on Electrode Materials for Lithium-Ion Batteries Using Spectroscopic Ellipsometry. *J. Electrochem. Soc.* **2012**, *159*, A198−A207.
(36) Tang, S. B.; Lai, M. O.; Lu, L.; Tripathy, S. Comparative study of LiMn2O4 thin film cathode grown at high, medium and low temperatures by pulsed laser deposition. *J. Solid State Chem.* **2006**, *179*, 3831−3838.
(37) Julien, C. M.; Massot, M. Lattice Vibrations of Materials for Lithium Rechargeable Batteries III. Lithium Manganese Oxides. *Mater. Sci. Eng., B* **2003**, *100*, 69−78.
(38) Quan, Z.; Ohguchi, S.; Kawase, M.; Tanimura, H.; Sonoyama, N. Preparation of Nanocrystalline LiMn2O4 Thin Film by Electrodeposition Method and Its Electrochemical Performance for Lithium Battery. *J. Power Sources* **2013**, *244*, 375−381.
(39) Molenda, M.; Dziembaj, R.; Podstawka, E.; Proniewicz, L. M. Changes in Local Structure of Lithium Manganese Spinels (Li:Mn=1:2) Characterised by XRD, DSC, TGA, IR, and Raman Spectroscopy. *J. Phys. Chem. Solids* **2005**, *66*, 1761−1768.
(40) Chiabrera, F.; Garbayo, I.; López-Conesa, L.; Martín, G.; Ruiz-Caridad, A.; Walls, M.; Ruiz-González, L.; Kordatos, A.; Núñez, M.; Morata, A.; Estradé, S.; Chroneos, A.; Peiró, F.; Tarancón, A. Engineering Transport in Manganites by Tuning Local Non-stoichiometry in Grain Boundaries. *Adv. Mater.* **2019**, *31*, 1805360.
(41) Julien, C. M.; Massot, M.; Poinsignon, C. Lattice vibrations of manganese oxides. *Spectrochim. Acta, Part A* **2004**, *60*, 689−700.
(42) Mironova-Ulmane, N.; Kuzmin, A.; Grube, M. Raman and Infrared Spectromicroscopy of Manganese Oxides. *J. Alloys Compd.* **2009**, *480*, 97−99.
(43) Wada, K.; Hyodo, T. A Simple Shape-Free Model for Pore-Size Estimation with Positron Annihilation Lifetime Spectroscopy. *J. Phys. Conf. Ser.* **2013**, *443*, 012003.
(44) Arabolla Rodríguez, R.; Della Santina Mohallem, N.; Avila Santos, M.; Sena Costa, D. A.; Andrey Montoro, L.; Mosqueda Laffita, Y.; Tavera Carrasco, L. A.; Perez-Cappe, E. L. Unveiling the Role of Mn-Interstitial Defect and Particle Size on the Jahn-Teller Distortion of the LiMn2O4 Cathode Material. *J. Power Sources* **2021**, *490*, 229519.
(45) Rougier, A.; Striebel, K. A.; Wen, S. J.; Cairns, E. J. Cyclic Voltammetry of Pulsed Laser Deposited Li x Mn2 O 4 Thin Films. *J. Electrochem. Soc.* **1998**, *145*, 2975.
(46) Thackeray, M. M.; David, W. I. F.; Bruce, P. G.; Goodenough, J. B. Lithium Insertion Into Manganese Spinels. *Mater. Res.* **1983**, *18*, 461−472.
(47) Raju, K.; Nkosi, F. P.; Viswanathan, E.; Mathe, M. K.; Damodaran, K.; Ozoemena, K. I. Microwave-Enhanced Electrochemical Cycling Performance of the LiNi0.2Mn1.8O4 Spinel Cathode Material at Elevated Temperature. *Phys. Chem. Chem. Phys.* **2016**, *18*, 13074−13083.
(48) Müller, H. A.; Joshi, Y.; Hadjixenophontos, E.; Peter, C.; Csiszár, G.; Richter, G.; Schmitz, G. High capacity rock salt type Li2MnO3−δthin film battery electrodes. *RSC Adv.* **2020**, *10*, 3636−3645.
(49) Susai, F. A.; Talianker, M.; Liu, J.; Rosy; Paul, T.; Grinblat, Y.; Erickson, E.; Noked, M.; Burstein, L.; Frenkel, A. I.; Tsur, Y.; Markovsky, B.; Aurbach, D. Electrochemical Activation of Li2MnO3 Electrodes at 0 °C and Its Impact on the Subsequent Performance at Higher Temperatures. *Materials* **2020**, *13*, 4388.
(50) Guerrini, N.; Jin, L.; Lozano, J. G.; Luo, K.; Sobkowiak, A.; Tsuruta, K.; Massel, F.; Duda, L.-C.; Roberts, M. R.; Bruce, P. G. Charging Mechanism of Li2MnO3. *Chem. Mater.* **2020**, *32*, 3733−3740.
(51) Ebin, B.; Battaglia, V.; Gürmen, S. Comparison of 4V and 3V electrochemical properties of nanocrystalline LiMn2O4 cathode particles in lithium ion batteries prepared by ultrasonic spray pyrolysis. *Ceram. Int.* **2014**, *40*, 7029−7035.
(52) Okubo, M.; Mizuno, Y.; Yamada, H.; Kim, J.; Hosono, E.; Zhou, H.; Kudo, T.; Honma, I. Fast Li-Ion Insertion into Nanosized LiMn2O4 without Domain Boundaries. *ACS Nano* **2010**, *4*, 741−752.
(53) Ohzuku, T.; Kitagawa, M.; Hirai, T. Electrochemistry of Manganese Dioxide in Lithium Nonaqueous Cell: III . X-Ray Diffractional Study on the Reduction of Spinel-Related Manganese Dioxide. *J. Electrochem. Soc.* **1990**, *137*, 769−775.
(54) Song, B.; Veith, G. M.; Park, J.; Yoon, M.; Whitfield, P. S.; Kirkham, M. J.; Liu, J.; Huq, A. Metastable Li1+δMn2O4 ($0 \leq \delta \leq 1$) Spinel Phases Revealed by in Operando Neutron Diffraction and First-Principles Calculations. *Chem. Mater.* **2019**, *31*, 124−134.
(55) Van Der Ven, A.; Marianetti, C.; Morgan, D.; Ceder, G. Phase Transformations and Volume Changes in Spinel LixMn2O4. *Solid State Ionics* **2000**, *135*, 21−32.

https://doi.org/10.1021/acsami.2c10798
ACS Appl. Mater. Interfaces 2022, 14, 33438−33446